JOURNAL OF SPACECRAFT AND ROCKETS
Vol. 35, No. 5, September–October 1998

Navier–Stokes Predictions of the Individual Components of the Pitch-Damping Sum

Paul Weinacht*
U.S. Army Research Laboratory, Aberdeen Proving Ground, Maryland 21005

An approach for predicting the two individual aerodynamic damping coefficients that form the pitch-damping coefficient sum is presented. The coefficients are obtained using prescribed or forced motions that independently excite the two different angular rates that are associated with the two damping coefficients. A key feature of the approach is that steady flowfields are produced by the selected motions. Steady flow computational fluid dynamics approaches can be applied, allowing results to be obtained in a computationally efficient manner. Application of the technique is made to an axisymmetric projectile configuration. The predicted pitch-damping coefficient sum obtained by adding the individually determined coefficients is in excellent agreement with previous predictions of the pitch-damping coefficient sum and with experimental data. The individual coefficients are compared with slender-body theory, and the results show similar trends though the slender-body theory appears to underpredict the various coefficients.

Nomenclature

C_m = pitching moment coefficient
C_{m_q} = damping moment coefficient due to transverse angular velocity
$C_{m_q} + C_{m_{\dot\alpha}}$ = pitch-damping moment coefficient sum
C_{m_α} = slope of the pitching moment coefficient with angle of attack
$C_{m_{\dot\alpha}}$ = damping moment coefficient due to angular rate of angle of attack
C_{N_q} = damping force coefficient due to transverse angular velocity
$C_{N_q} + C_{N_{\dot\alpha}}$ = pitch-damping force coefficient sum
$C_{N_{\dot\alpha}}$ = damping force coefficient due to angular rate of angle of attack
C_n = side moment coefficient
$C_{n_{p\alpha}}$ = Magnus moment coefficient
D = projectile diameter
$\hat{\boldsymbol{E}}$, $\hat{\boldsymbol{F}}$, $\hat{\boldsymbol{G}}$ = flux vectors in transformed coordinates
e = total energy per unit volume
$\hat{\boldsymbol{H}}$ = source term in Navier–Stokes (N–S) equations
J = Jacobian
l = characteristic length, typically D
M = freestream Mach number
p = pressure, as used in N–S equations; spin rate, as used in roll equations
Re = Reynolds number, $a_\infty \rho_\infty D/\mu_\infty$
R_0 = helix radius or radius of circular arc for looping motion
r = radial coordinate
$\hat{\boldsymbol{S}}$ = viscous flux vector
s = distance downrange
s_{cg} = center of gravity shift, calibers
t = time
U = vehicle velocity along helix axis
u, v, w = velocity components in x, y, z directions
V = freestream velocity
x, y, z = axial, horizontal, and vertical coordinates
x_{cg} = axial location of body center of gravity
α = angle of attack
γ = ratio of specific heats, in N–S equations; cosine of total angle of attack, as used in aerodynamic force and moment equations
δ = sine of total angle of attack
μ, μ_t = laminar and turbulent viscosity
$\tilde{\mu}$ = complex transverse angular velocity
ξ, η, ζ = transformed coordinates in N–S equations
$\tilde{\xi}$ = complex yaw
ρ = density
ϕ = circumferential coordinate, measured from vertical axis
Ω = angular rate associated with looping and helical motions

Superscripts

$\cdot$ = rate of change with respect to time
$'$ = rate of change with respect to space
$\tilde{}$ = referenced to nonrolling coordinate frame

Introduction

TRADITIONALLY in aeroballistic applications, the pitch-damping coefficient has been treated as the sum of two individual coefficients that produce an aerodynamic moment proportional to the angular rate associated with the angle of attack. In fact, these two individual coefficients represent moments proportional to two different angular rates, although for many nonmanuevering flight trajectories, including those flown in ballistic aerodynamic ranges, these two angular rates are essentially equivalent. For this reason, the pitch-damping coefficient sum is often treated as a single parameter. In some cases, such as for manuevering flight vehicles, the simplification that the two angular rates are equivalent is no longer valid, and the two individual components of the pitch-damping coefficient sum must be determined independently. Experimental determination of these coefficients is difficult at best and is probably not possible using traditional aerodynamic ranges.

Prior research has focused on the development and application of computational methods for predicting the pitch-damping coefficient sum. The basis of the technique is to impose a particular motion (coning motion) on the flight vehicle, which produces moments that are proportional to the pitch-damping coefficient sum. Because coning motion produces a steady flowfield in the cases of interest, efficient numerical techniques can be readily applied and the pitch-damping coefficient sum determined in a cost-efficient manner. These techniques have been benchmarked with experimental data, and good agreement between computation and experiment has been found for a number of flight vehicle geometries.[1–8]

Received Aug. 12, 1997; revision received June 18, 1998; accepted for publication July 2, 1998. This paper is declared a work of the U.S. Government and is not subject to copyright protection in the United States.

*Aerospace Engineer, Aerodynamics Branch, Propulsion and Flight Division, Weapons and Materials Research Directorate. Associate Fellow AIAA.

In the current effort, the method is extended so that the individual components of the pitch-damping coefficient can be determined independently. The method uses imposed motions that excite the two angular rates independently so that the forces and moments attributable to these rates can be assessed separately. A key feature of the approach is that the motions produce steady flowfields that can be computed in a cost-efficient manner. The techniques described here represent a unique aerodynamic capability for a problem that is difficult to address experimentally. Other than approximate methods, these results most likely represent the first theoretical predictions of the individual components of the pitch-damping coefficient sum for flight vehicles. Subsequent to its original publication,[7,8] the technique has also been adopted by other researchers.[9]

This paper presents a derivation of the transverse aerodynamic force and moment equations associated with the motions of interest using a general force and moment expansion for symmetric flight bodies. The resulting equations demonstrate that the aerodynamic forces and moments can be excited independently using the appropriate motions. Results are presented for an axisymmetric flight body at supersonic flight velocities. Both of the components (C_{m_q} and $C_{m_{\dot\alpha}}$) of the pitch-damping coefficient sum ($C_{m_q}+C_{m_{\dot\alpha}}$) are determined independently. Comparison of the predicted aerodynamic coefficients is made with slender-body theory. The sum of the two individually determined coefficients is also compared with the pitch-damping coefficient sum ($C_{m_q}+C_{m_{\dot\alpha}}$) determined from coning motion. Both methods of determining the pitch-damping coefficient sum are in good agreement with experimental data.

Theoretical Background

Force and Moment Expansion

It is common in many aerodynamics applications to use a body-fixed, nonrolling coordinate system to describe both the dynamics and the system of forces and moments that act on the flight vehicle.[10] The nonrolling coordinate system allows the description of the vehicle dynamics to be simplified for certain classes of flight vehicles that possess particular types of geometric symmetry. Rotationally symmetric flight vehicles, which are the focus of the current research, represent one class of vehicles where the nonrolling frame has been effectively (and traditionally) used. For more complicated geometries, such as aircraft, the advantages of the nonrolling frame are reduced, and other coordinate frames such as a completely body-fixed coordinate system are typically used.

In the current effort, the primary reason for initially describing the aerodynamic forces and moments using the nonrolling coordinate system is the description is well established for symmetric flight vehicles. The nonrolling coordinate frame is an orthogonal right-handed system ($\tilde{x}$, $\tilde{y}$, $\tilde{z}$) centered at the body c.g. The $\tilde{x}$ axis is aligned along the projectile longitudinal axis with the positive direction oriented toward the projectile nose. The $\tilde{z}$ axis is initially oriented downward with the $\tilde{x}$–$\tilde{z}$ plane perpendicular to the ground. The angular motion of the nonrolling coordinate frame is such that, with respect to an inertial frame, the $\tilde{x}$ component of the coordinate frame's angular velocity is zero. Although the time-dependent orientation of the nonrolling frame may be difficult to visualize, the nonrolling frame is essentially equivalent to the fixed-plane coordinate system for small amplitude motions. In the fixed-plane coordinate system, the $\tilde{x}$–$\tilde{z}$ plane remains perpendicular to the ground for all time. The total angular velocity of the flight vehicle can be described in terms of its angular velocity components (p, $\tilde{q}$, and $\tilde{r}$) along the $\tilde{x}$, $\tilde{y}$, and $\tilde{z}$ axes, respectively. The angular velocity of the nonrolling frame can be described in terms of the transverse angular velocities $\tilde{q}$ and $\tilde{r}$ because the angular velocity of the nonrolling frame along the $\tilde{x}$ axis is always zero. The flight body may, however, have a nonzero spin rate p about its longitudinal axis. Further details about these coordinate frames are discussed in Ref. 10.

The moment expansion for a rotationally symmetric missile in the nonrolling coordinate frame is

$$\tilde{C}_m + i\tilde{C}_n = \left[(pl/V)C_{n_{p\alpha}} - iC_{m_\alpha}\right]\tilde{\xi} + C_{m_q}\tilde{\mu} - iC_{m_{\dot\alpha}}\tilde{\xi}' \qquad (1)$$

This moment expansion is similar to the moment proposed by Murphy.[10] The moment formulation uses complex variables to separate the moment components, $\tilde{C}_m$ and $\tilde{C}_n$, that are oriented along the $\tilde{y}$ and $\tilde{z}$ axes, respectively. The third moment component, the roll moment, can be handled separately and is not of consequence in this study.

In the moment expansion, the pitching moment coefficient slope C_{m_α} and the coefficient $C_{m_{\dot\alpha}}$ represent moments that are proportional to the complex yaw $\tilde{\xi}$ and yawing rate $\tilde{\xi}'$, respectively. The complex yaw and yawing rate are

$$\tilde{\xi} = (\tilde{v} + i\tilde{w})/V \qquad (2)$$

$$\tilde{\xi}' \equiv \frac{\mathrm{d}\tilde{\xi}}{\mathrm{d}(s/l)} \qquad (3)$$

(In the analysis presented here, there is no need to distinguish between pitch and yaw, and the terms may be interchanged. The usage follows that of Murphy.[10]) Here, $\tilde{v}$ and $\tilde{w}$ are the $\tilde{y}$ and $\tilde{z}$ components of the velocity vector $\boldsymbol{V}$ that describes the velocity of the body c.g. relative to the inertial frame. The magnitude of this vector is denoted as V. The angular rate is obtained by taking the derivative of the complex yaw with respect to the flight-path coordinate s, which is nondimensionalized by some characteristic length l, typically the body diameter.

The coefficient C_{m_q} represents a moment that is proportional to the complex transverse angular velocity of the vehicle $\tilde{\mu}$

$$\tilde{\mu} = \frac{(\tilde{q} + i\tilde{r})l}{V} \qquad (4)$$

where $\tilde{q}$ and $\tilde{r}$ are the $\tilde{y}$ and $\tilde{z}$ components of angular velocity of the vehicle in the nonrolling coordinate system. The remaining coefficient in the moment expansion, the Magnus moment coefficient $C_{n_{p\alpha}}$ accounts for a side moment due to flow asymmetries produced by the combination of spin and yaw.

Note that the moment formulation neglects the variation of the moments with roll angle under the assumption that these variations are small. For axisymmetric vehicles, the variations with roll angle should not exist because the geometry will not change as the roll orientation changes. Roll variations in the aerodynamic coefficients for other types of rotationally symmetric vehicles are typically negligible for small amplitude motions. In general, roll variations may be difficult to detect in flight because the effect of roll orientation tends to be averaged out over the course of a yaw cycle if the body is spinning.

Planar Motions

For planar motions, the aerodynamic moments that act on an axisymmetric flight body can be written in terms of the following expansion:

$$\tilde{C}_m + i\tilde{C}_n = \left[i(pl/V)C_{n_{p\alpha}} + C_{m_\alpha}\right]\sin\alpha + C_{m_q}(ql/V) + \gamma C_{m_{\dot\alpha}}(\dot\alpha l/V) \qquad (5)$$

The force expansion has a similar form. Two damping moments, $C_{m_{\dot\alpha}}$ and C_{m_q}, represent moments proportional to the angular rates $\dot\alpha$ and q that are associated with the angle of attack α and the angular displacement of the longitudinal axis of the body with respect to the Earth-fixed axis system denoted by the angle θ, respectively. These angles are displayed schematically in Fig. 1 for the case of planar motion.

For a typical ballistic trajectory, over the course of many yaw cycles, the flight body will travel a nearly rectilinear flight path. In this case, the freestream velocity vector $\boldsymbol{V}_\infty$ has a fixed orientation

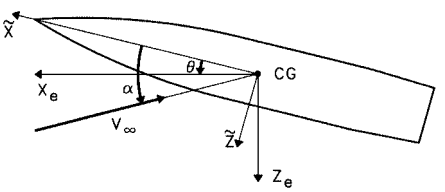

Fig. 1 Angular orientation of projectile relative to velocity vector and Earth-fixed coordinate frame.

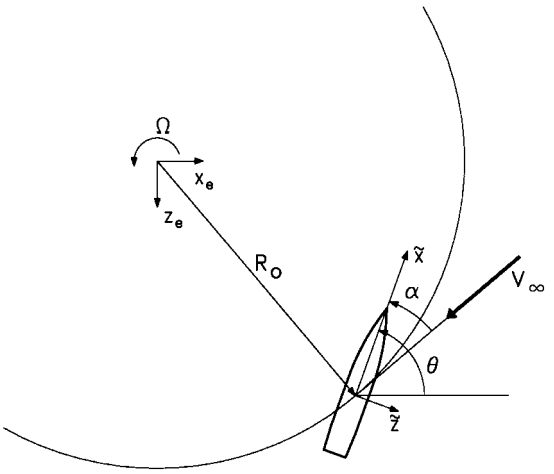

Fig. 2 Schematic of planar looping motion.

with respect to the Earth-fixed axes, x_e and z_e. For a rectilinear flight path, the angular rates $\dot{\alpha}$ and q will be equal. The moment expansion can be simplified by combining the two damping coefficients into a single coefficient sum, which is proportional to a single angular rate (either $\dot{\alpha}$ or q). For maneuvering flight bodies, this simplification may not be valid and the individual coefficients must be treated independently.

To produce aerodynamic moments proportional to the damping terms, one or both of the angular velocities must be nonzero. One simple planar motion that produces a nonzero q and zero $\dot{\alpha}$ angular velocity is a circular looping motion, as shown in Fig. 2. If such a motion is performed at constant angular velocity Ω, where $q = \dot{\theta} = \Omega$, and constant angle of attack (which may or may not be zero), the following form of the force and moment expansions results:

$$\tilde{C}_m + i\tilde{C}_n = \left[i(pl/V)C_{n_{p\alpha}} + C_{m_\alpha}\right]\sin\alpha + C_{m_q}(\Omega l/V) \qquad (6)$$

where the in-plane moment C_m contains contributions from both the pitching moment slope C_{m_α} and the pitch-damping coefficient C_{m_q}. The side moment C_n is identical in form to the side moment due to constant α motion and is independent of the angular rate q. Because the damping terms are independent of the spin rate and the side moment is independent of the angular rate q, the spin rate is assumed to be zero to simplify the discussion of the looping motion that follows.

With respect to the inertial frame of reference, the flowfield is periodic and unsteady. However, in the nonrolling frame (shown in Fig. 2 as the $\tilde{x}$–$\tilde{z}$ axes), the flowfield is potentially steady. Indeed, the moment expansion displays no unsteadiness because all of the terms on the right-hand side are constants. Because the flowfield is potentially steady in the nonrolling frame for this type of motion, this frame is suitable for use with computational approaches that are based on steady flow techniques.

For looping motion, the moment expansion contains contributions from two of the aerodynamic coefficients. The contribution from the pitching moment coefficient slope C_{m_α} can be eliminated if the body longitudinal axis is tangent to the radius of curvature of the loop. In this case, the angle of attack is zero, and the damping moment C_{m_q} is directly proportional to the net aerodynamic moment. If the damping moment exhibits a dependence on angle of attack, several experiments or computations involving different looping rates must be performed for each angle of attack. (If the looping rate is varied, the loop radius must also be changed to maintain a constant vehicle velocity, $V = \Omega R_0$.) The damping moment can be obtained by computing the variation in the net aerodynamic moment with looping rate. If the net aerodynamic moment displays a nonlinear variation with both angle of attack and looping rate, it may be difficult to separate the contributions attributable to the C_{m_α} and C_{m_q}, without additional information or assumptions. In general, variations of the coefficients with angle of attack might be reasonably expected, whereas variations in the coefficients with angular rate are less common. In any event, the looping motion can be used to check for these types of nonlinear variations.

One feature of this type of motion is that high angular velocities or large loop radii are required to generate high velocities, making this type of motion impractical for use in experimental testing. However, this is not a problem for computational approaches because large loop radii or high angular velocities can be easily accommodated.

Helical Motions

Other more complicated motions can be proposed, which produce aerodynamic moments proportional to the angular rates $\tilde{\mu}$ and $\tilde{\xi}'$, nevertheless still producing steady flowfields when viewed from the appropriate coordinate frame. Two such motions require the c.g. of the flight vehicle to traverse a helical flight path. The first motion requires the vehicle's longitudinal axis to be oriented in the same direction as the center of rotation of the helix but displaced by a constant distance. Figure 3 shows a three-dimensional view of the motion.

A two-dimensional projection of this motion on the vertical plane is shown in Fig. 4. This particular motion produces no rotation of the nonrolling coordinate frame relative to an Earth-fixed coordinate frame, and hence, the angular velocity $\tilde{\mu}$ is zero. The angle of attack and its angular rate vary continuously, producing moment components associated with the coefficients C_{m_α} and $C_{m_{\dot{\alpha}}}$, respectively. This motion is referred to as $q = 0$ helical motion because the angular rates associated with the damping coefficient C_{m_q} are zero.

For the second motion, the longitudinal axis of the flight vehicle remains tangent to the helical flight path at each point along the trajectory. Figure 5 shows a three-dimensional view of this motion. A two-dimensional projection of this motion on the vertical plane is also shown in Fig. 6. The angle of attack of the incident airstream is zero because both the longitudinal axis of the body and the freestream velocity vector are tangent to the flight path. The resulting yawing rate is also zero because the angle of attack is constant. The angular orientation of the flight body changes

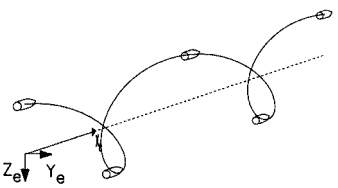

Fig. 3 Helical motion with nonzero $\tilde{\alpha}$ and zero $\tilde{q}$.

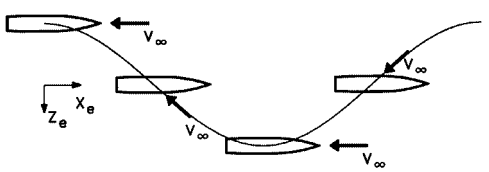

Fig. 4 Vertical projection of helical motion with nonzero $\tilde{\alpha}$ and zero $\tilde{q}$.

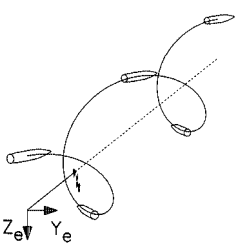

Fig. 5 Helical motion with zero $\tilde{\alpha}$ and nonzero $\tilde{q}$.

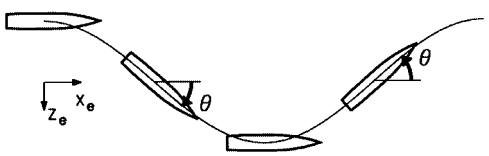

Fig. 6 Vertical projection of helical motion with zero $\tilde{\alpha}$ and nonzero $\tilde{q}$.

continuously with respect to an Earth-fixed reference frame, producing a nonzero angular rate $\tilde{\mu}$. As a result, moment components associated with the damping moment C_{m_q} are produced. This motion is referred to as $\dot{\alpha} = 0$ helical motion because the angular rates associated with the damping coefficient $C_{m_{\dot{\alpha}}}$ are zero. The $\dot{\alpha} = 0$ helical motion produces a steady flowfield when viewed from the appropriate coordinate system, whereas its two-dimensional projection is clearly time dependent.

The net transverse aerodynamic moment in the nonrolling frame can be determined for each of the motions by substituting the appropriately determined angle of attack and angular rates $\tilde{\xi}'$ and $\tilde{\mu}$ into Eq. (1).

For $q = 0$ helical motion

$$\tilde{\xi} \equiv (\tilde{v} + i\tilde{w})/V = -\delta e^{i\Omega t} \tag{7}$$

$$\delta = \frac{R_0\Omega}{\sqrt{U^2 + \Omega^2 R_0^2}} \tag{8}$$

$$\tilde{\xi}' = -i(\Omega l/V)\delta e^{i\Omega t} \tag{9}$$

$$\tilde{\mu} = 0 \tag{10}$$

For $\dot{\alpha} = 0$ helical motion

$$\tilde{\mu} \equiv \frac{(\tilde{q} + i\tilde{r})l}{V} = \frac{\Omega l}{V}(\sin\beta)e^{i\Omega t\cos\beta} \tag{11}$$

$$\cos\beta = U/V \tag{12}$$

$$\sin\beta = R_0\Omega/V \tag{13}$$

$$\tilde{\xi} = \tilde{\xi}' = 0 \tag{14}$$

where Ω is the angular velocity of the body about the helix axis, R_0 is the perpendicular distance between the helix axis and the body c.g., U is the component of velocity along the helix axis, and V is the total linear velocity of the c.g. To eliminate the contribution to the net aerodynamic moment from the Magnus moment, it is assumed that the spin rate of the vehicle is zero.

For each of the helical motions, the transverse aerodynamic moment in the nonrolling frame will be periodic in time, which also indicates that the flowfield will be periodic in time when viewed from the nonrolling coordinate frame. However, for both types of helical motion, a steady flowfield should be observed when examined from an orthogonal right-handed coordinate system that has its x axis aligned with the longitudinal axis of the body and its z axis along a line between the body c.g. and the axis of rotation of the helix. The transverse aerodynamic moments in the nonrolling frame can be transformed to the coordinate frame where the steady flowfield exists, using the following relations:

For $q = 0$ helical motion

$$C_m + iC_n = (\tilde{C}_m + i\tilde{C}_n)e^{-i\Omega t} \tag{15}$$

For $\dot{\alpha} = 0$ helical motion

$$C_m + iC_n = (\tilde{C}_m + i\tilde{C}_n)e^{-i\Omega t\cos\beta} \tag{16}$$

where the transverse moments C_m and C_n refer to the moments about the y and z axes, respectively.

Using this transformation, the transverse moments can be shown to have the following form for each of the two types of helical motion:

For $q = 0$ helical motion

$$C_m + iC_n = -C_{m_{\dot{\alpha}}}(\Omega l/V)(R_0\Omega/V) + iC_{m_\alpha}(R_0\Omega/V) \tag{17}$$

For $\dot{\alpha} = 0$ helical motion

$$C_m + iC_n = C_{m_q}(\Omega l/V)(R_0\Omega/V) \tag{18}$$

The resulting expressions for the transverse moments are independent of time, indicating that the flowfield is potentially steady as well.

Similar expressions for the individual damping force coefficients can be developed using the same approach as applied for the moment coefficients.

For $q = 0$ helical motion

$$C_Y + iC_Z = iC_{N_{\dot{\alpha}}}(\Omega l/V)\delta + C_{N_\alpha}\delta \tag{19}$$

For $\dot{\alpha} = 0$ helical motion

$$C_Y + iC_Z = -iC_{N_q}(\Omega l/V)\sin\beta \tag{20}$$

Center of Gravity Translation Relations

If the aerodynamic coefficients have been established for a baseline configuration, it is possible to determine the aerodynamic coefficients for the identical configuration that has a different axial c.g. location using the c.g. translation relations.[10] The c.g. translation relations for the damping coefficients are

$$\hat{C}_{N_{\dot{\alpha}}} = C_{N_{\dot{\alpha}}} \tag{21}$$

$$\hat{C}_{N_q} = C_{N_q} + s_{\mathrm{cg}}C_{N_\alpha} \tag{22}$$

$$\hat{C}_{m_{\dot{\alpha}}} = C_{m_{\dot{\alpha}}} - s_{\mathrm{cg}}C_{N_{\dot{\alpha}}} \tag{23}$$

$$\hat{C}_{m_q} = C_{m_q} - s_{\mathrm{cg}}\left(C_{N_q} - C_{m_\alpha}\right) - s_{\mathrm{cg}}^2 C_{N_\alpha} \tag{24}$$

In the context of the current study, the c.g. translation relations can be used to further validate the results by comparing the theoretical variation of the damping coefficients with c.g. location with the computational fluid dynamics predictions.

Computational Approach

Computation of the viscous flowfield about the flight body was accomplished by solving the thin-layer Navier–Stokes equations using a parabolized Navier–Stokes technique (PNS). Because the computations are performed in a noninertial rotating coordinate frame, the governing equations have been modified to include the body force terms that result from the Coriolis and centripedal accelerations in the rotating coordinate frame. The fluid flow relative to the rotating coordinate frame does not vary with time, allowing the steady (nontime-varying) Navier–Stokes equations to be applied. The solution of the steady Navier–Stokes equations can be performed at a reasonable computational cost. To implement the rolling coordinate frame, the governing equations were modified to include the effects of centrifugal and Coriolis forces. The steady thin-layer Navier–Stokes equations are

$$\frac{\partial\hat{\boldsymbol{E}}}{\partial\xi} + \frac{\partial\hat{\boldsymbol{F}}}{\partial\eta} + \frac{\partial\hat{\boldsymbol{G}}}{\partial\zeta} + \hat{\boldsymbol{H}}_c + \hat{\boldsymbol{H}} = \frac{1}{Re}\left(\frac{\partial\hat{\boldsymbol{S}}}{\partial\zeta} + \hat{S}_c\right) \tag{25}$$

where $\hat{\boldsymbol{H}}_c$ and $\hat{\boldsymbol{S}}_c$ are inviscid and viscous source terms due to the cylindrical coordinate formulation and $\hat{\boldsymbol{H}}$ is the source term containing the Coriolis and centrifugal force terms that result from the rotating coordinate frame. Each of these matrices is a function of the dependent variables represented by the vector $\boldsymbol{q}(\rho, \rho u, \rho v, \rho w, e)$, where ρ and e are the density and the total energy per unit volume

and u, v, and w, are the velocity components in the axial, circumferential, and normal directions. The flux terms are

$$\hat{\boldsymbol{E}} = \frac{1}{J}\begin{bmatrix} \rho U \\ \rho u U + \xi_x p \\ \rho v U \\ \rho w U \\ (e+p)U \end{bmatrix}, \qquad \hat{\boldsymbol{H}} = \frac{1}{J}\begin{bmatrix} 0 \\ \rho f_x \\ \rho f_\phi \\ \rho f_r \\ (\rho u f_x + \rho v f_\phi + \rho w f_r) \end{bmatrix} \tag{26}$$

$$\hat{\boldsymbol{F}} = \frac{1}{J}\begin{bmatrix} \rho V \\ \rho u V + \eta_x p \\ \rho v V + \eta_\phi p/r \\ \rho w V + \eta_r p \\ (e+p)V \end{bmatrix}, \qquad \hat{\boldsymbol{G}} = \frac{1}{J}\begin{bmatrix} \rho W \\ \rho u W + \zeta_x p \\ \rho v W + \zeta_\phi p/r \\ \rho w W + \zeta_r p \\ (e+p)W \end{bmatrix}$$

where

$$U = u\xi_x, \qquad V = u\eta_x + v\eta_\phi/r + w\eta_r$$
$$W = u\zeta_x + v\zeta_\phi/r + w\zeta_r \tag{27}$$

$$\xi_x = 1/x_\xi, \qquad \eta_x = J(r_\xi \phi_\zeta - \phi_\xi r_\zeta), \qquad \eta_\phi = J(x_\xi r_\zeta)$$
$$\eta_r = J(-x_\xi \phi_\zeta), \qquad \zeta_x = J(\phi_\xi r_\eta - r_\xi \phi_\eta) \tag{28}$$
$$\zeta_\phi = J(-x_\xi r_\eta), \qquad \zeta_r = J(x_\zeta \phi_\eta), \qquad J = 1/[x_\xi(\phi_\eta r_\zeta - \phi_\zeta r_\eta)]$$

The Coriolis and centrifugal acceleration terms due to the rotating coordinate system that are contained in the source term $\hat{\boldsymbol{H}}$ are

$$\boldsymbol{f} = 2\boldsymbol{\Omega} \times \boldsymbol{u} + \boldsymbol{\Omega} \times (\boldsymbol{\Omega} \times \boldsymbol{R}) \tag{29}$$

The Coriolis acceleration is a function of the angular velocity of the coordinate frame with respect to the inertial frame $\boldsymbol{\Omega}$ and the fluid velocity vector $\boldsymbol{u}$, which can be represented by the velocity components u, v, and w. The centripedal acceleration is a function of the angular velocity of the rotating frame $\boldsymbol{\Omega}$ and the displacement vector $\boldsymbol{R}$ between the axis of rotation and the local position in the flowfield. The acceleration vector $\boldsymbol{f}$ can be written in terms of its components along the x, ϕ, and r axes, f_x, f_ϕ, and f_r.

The angular velocities for the three different motions considered are given next. The angular velocities are nondimensionalized in a manner consistent with the Navier–Stokes equations.

For looping motion

$$\boldsymbol{\Omega} = \left(\frac{\Omega D}{a_\infty}\right)\cos\phi \boldsymbol{i}_\phi - \left(\frac{\Omega D}{a_\infty}\right)\sin\phi \boldsymbol{i}_r \tag{30}$$

For $\dot{\alpha} = 0$ helical motion

$$\boldsymbol{\Omega} = \left(\frac{\Omega D}{a_\infty}\right)\boldsymbol{i}_x \tag{31}$$

For $q = 0$ helical motion

$$\boldsymbol{\Omega} = \left(\frac{\Omega D}{a_\infty}\right)\cos\beta \boldsymbol{i}_x + \left(\frac{\Omega D}{a_\infty}\right)\sin\beta\cos\phi \boldsymbol{i}_\phi$$
$$- \left(\frac{\Omega D}{a_\infty}\right)\sin\beta\sin\phi \boldsymbol{i}_r \tag{32}$$

The pressure p can be related to the dependent variables by applying the ideal gas law,

$$p = (\gamma - 1)[e - (\rho/2)(u^2 + v^2 + w^2)] \tag{33}$$

The turbulent viscosity μ_t, which appears in the viscous matrices, was computed using the Baldwin–Lomax turbulence model.[11]

The thin-layer equations are solved using the parabolized Navier–Stokes technique of Schiff and Steger.[12] Following the approach of Schiff and Steger, the governing equations, which have been modified here to include the Coriolis and centrifugal force terms, are solved using a conservative, approximately factored, implicit finite difference numerical algorithm as formulated by Beam and Warming.[13] Details of the implementation of the source term that contains the Coriolis and centrifugal force terms are given in Ref. 5.

The computations presented here were performed using a shock-fitting procedure.[14] This procedure solves the five Rankine–Hugoniot jump conditions, two geometric shock propagation conditions, and one compatibility equation to determine the values of the five dependent variables immediately behind the shock, as well as the position of the shock. By including the implicit part of the source term due to the rotating coordinate frame in the circumferential inversion, the shock-fitting procedure can be used without modification, as long as the freestream conditions are modified to account for the rotating coordinate frame.

At the body surface, no-slip, constant wall temperature boundary conditions were applied. For the cases with spin, the tangential velocity v was set equal to the local velocity of the body surface due to solid-body rotation.

An initial solution for the PNS marching procedure was obtained using a conical stepback procedure at a location of 0.2 body diameters from the nose tip. Although the perturbations to the flowfield from the helical motions are not compatible with the conical flow assumption, the effect on the solution appears to be small. Moving the starting plane to 0.1 body diameters from the nose tip resulted in less than 0.5% variation in the computed damping moments.

The computational results presented here were obtained using a grid that consisted of 60 points between the body and the shock. In the circumferential direction, gridding was performed over a 360-deg sector because of the lack of symmetry from the combination of angle of attack, spin, and coning or helical motion. In the circumferential direction 36 grid points were used. In the longitudinal direction, 78 marching steps were utilized for each body diameter of length. To ensure adequate grid resolution within the boundary layer, the grid spacing at the body surface was adapted to maintain nondimensional boundary-layer coordinate y^+ between 2 and 3 in accordance with previously published results.[15] Grid resolution studies for the 9-caliber body (middle c.g. location) showed less than 2% variation in the computed pitch-damping coefficient, when the grid resolution was decreased by 25% in each of the three coordinate directions. Similarly, when the grid in the circumferential and marching directions was doubled and the grid in the radial direction was increased by 50%, the computed pitch-damping coefficient varied by only 1%. Differences in the damping coefficient C_{m_q} on the coarse and fine mesh relative to the baseline grid were less than 1%. The damping coefficient $C_{m_{\dot{\alpha}}}$ showed a larger variability on a percentage basis on the coarse and fine grid relative to the baseline grid (6% and 3%, respectively), although absolute differences between the predicted values of the coefficient were similar to the differences between the predicted pitch-damping coefficient sum. The smaller magnitude of $C_{m_{\dot{\alpha}}}$ relative to the pitch-damping coefficient sum contributed to a larger percentage error. The computations for the baseline grid performed using a Cray Y-MP supercomputer typically required less than 10 min of CPU time for complete calculation over a single configuration.

Results

Computations of the individual coefficients that comprise the pitch-damping force and moment coefficient sums were performed using helical and looping motions. The computations were performed for the Army–Navy spinner rocket (ANSR) series of bodies shown in Fig. 7. Results for the $L/D = 5$ and $L/D = 9$ bodies are presented here for a flight velocity of Mach 2.5. Three different c.g. locations were considered for each body length, as shown in Table 1. Aerodynamic range tests of the ANSR[16] were used to benchmark the predicted pitch-damping coefficient sum.

Table 1 ANSR flight bodies c.g. location

	Longitudinal c.g. (calibers from nose)		
L/D	Forward	Middle	Rearward
5	2.5	3.0	3.5
9	4.0	5.038	5.885

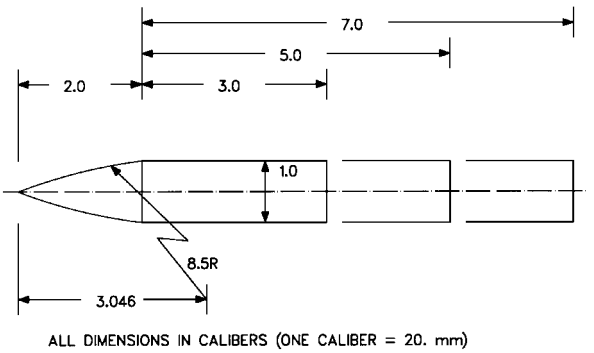

Fig. 7 Schematic of the ANSR.

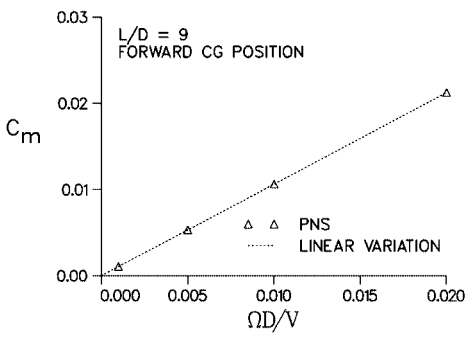

Fig. 8 Variation of aerodynamic moment C_m with angular velocity, $q = 0$ helical motion, $M = 2.5$, ANSR, $\sin^{-1}\delta = 2$ deg.

The effect of angular rate and rotational velocity ratio for the $q = 0$ helical motion and $\dot{\alpha} = 0$ helical motion was examined for the $L/D = 9$ ANSR body (forward c.g.) at a flight velocity of Mach 2.5. The force and moment expansion for both of these motions indicates that a linear variation of the forces and moments is expected with angular rate and rotational velocity ratio within the regime where linear aerodynamic theory is expected to be valid. The predictions were performed for the longest ANSR body because the longer bodies typically exhibit more nonlinear aerodynamic behavior. Thus, the onset of nonlinear behavior of the aerodynamics with angular rate or angle of attack would be more evident, and the limits of linear aerodynamic behavior could be more readily identified.

The effect of angular rate for the $q = 0$ motion was examined by performing computations at several angular velocities but at a fixed total angle of attack of 2 deg. This means that as the angular velocity was increased, the radius R_0 was decreased so that the product $R_0\Omega$ (and the total angle of attack) was constant. Figure 8 shows the variation of the aerodynamic moment C_m with angular velocity, and the variation is seen to be linear across the range of angular velocities of interest.

For the $q = 0$ helical motion, the sine of the angle of attack, δ, varies directly with the rotational velocity ratio $\Omega R_0/V$. Thus, as the rotational velocity ratio increases toward 1, the angle of attack of the vehicle also increases for the $q = 0$ helical motion. (In the limit as $\Omega R_0/V = 1$, for $q = 0$ helical motion, the c.g. performs a circular looping motion with the body at 90-deg angle of attack.) The desire is to define the limits where the forces and moments are expected to vary linearly with δ or $\Omega R_0/V$. Computations of $q = 0$ helical motion were performed with the angular rate held fixed ($\Omega D/V = 0.010$) while the helix radius was varied to produce the desired angle of attack. The aerodynamic moment C_m, shown in Fig. 9, shows a linear variation with δ up to angles of attack of about 7 deg. This behavior is similar to that observed for coning motion.[5]

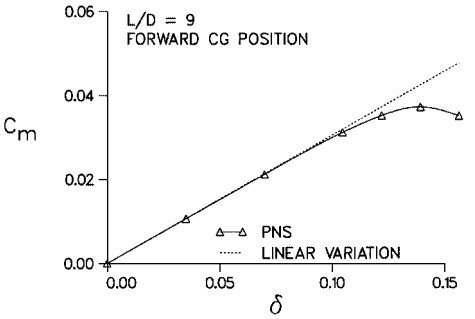

Fig. 9 Variation of aerodynamic moment C_m with sine of the angle of attack, $q = 0$ helical motion, $M = 2.5$, ANSR, $\Omega D/V = 0.010$.

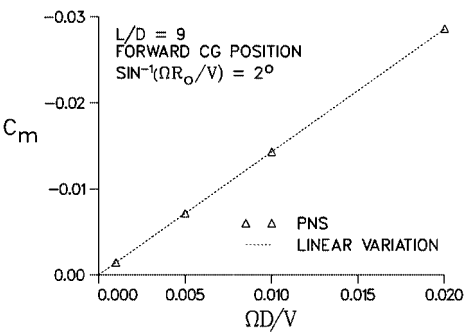

Fig. 10 Variation of aerodynamic moment C_m with angular velocity, $\dot{\alpha} = 0$ helical motion, $M = 2.5$, ANSR, $\beta = 2$ deg.

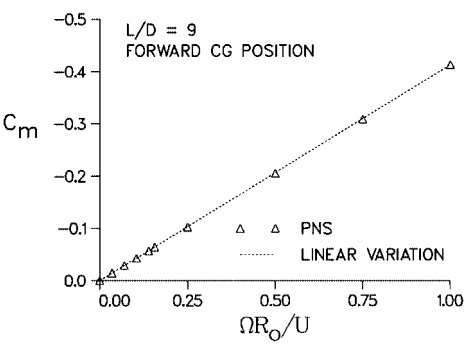

Fig. 11 Variation of aerodynamic moment C_m with rotational velocity ratio, $\dot{\alpha} = 0$ helical motion, $M = 2.5$, ANSR, $\Omega D/V = 0.010$.

For the $\dot{\alpha} = 0$ helical motion, the effect of angular rate was examined for rotational velocity ratio, $\Omega R_0/V = \sin\beta = 0.0349$. Again, as the angular velocity was increased, the radius R_0 was decreased so that the product $R_0\Omega$ (and the total angle of attack) was constant. The variation of the aerodynamic moment C_m with angular velocity, shown in Fig. 10, is seen to be linear across the range of angular velocities of interest.

The effect of the rotational velocity ratio on the forces and moments for the $\dot{\alpha} = 0$ helical motion was also examined, and the results are shown in Fig. 11. These predictions were made for a constant angular velocity ($\Omega D/V = 0.010$). The aerodynamic moment C_m is seen to be linear with rotational velocity ratios from 0 to 1. At first glance, a nonlinear variation might be expected because nonlinear variations with δ were seen for the $q = 0$ helical motion. It is noted that the parameter $\Omega R_0/V = \sin\beta$ is not associated with the angle of attack for this motion because the $\dot{\alpha} = 0$ helical motion is performed at 0-deg angle of attack. The parameter $\sin\beta$ is simply the rotational velocity ratio. The limiting case of a rotational velocity ratio of 1 corresponds to a circular looping motion discussed earlier.

Using these results as a guide, predictions of the pitch-damping coefficients were made for each of the three body lengths and c.g.s at Mach 1.8 and 2.5. Predictions were made at an angular velocity of

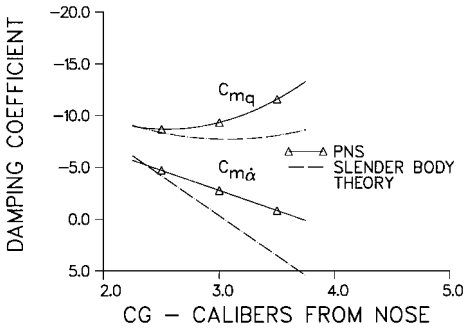

Fig. 12 Variation of damping moment coefficients with c.g. location, M = 2.5, ANSR, L/D = 5.

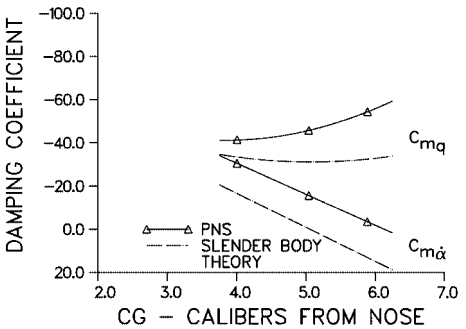

Fig. 13 Variation of damping moment coefficients with c.g. location, M = 2.5, ANSR, L/D = 9.

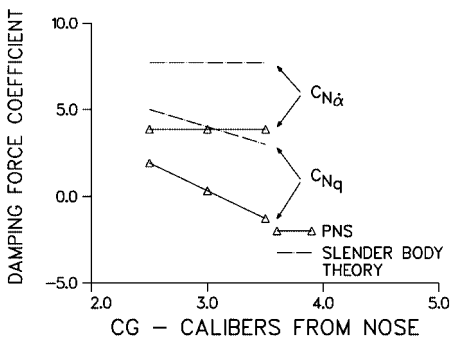

Fig. 14 Variation of pitch-damping force coefficients with c.g. location, M = 2.5, ANSR, L/D = 5.

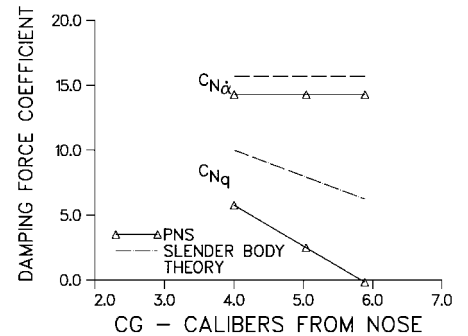

Fig. 15 Variation of pitch-damping force coefficients with c.g. location, M = 2.5, ANSR, L/D = 9.

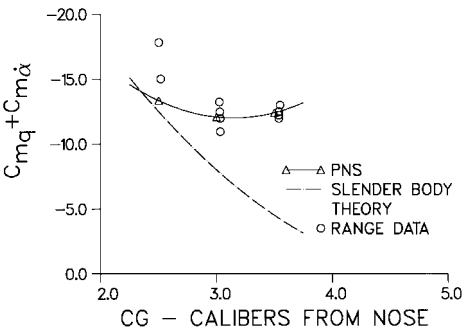

Fig. 16 Variation of pitch-damping moment coefficient sum with c.g. location, M = 2.5, ANSR, L/D = 5.

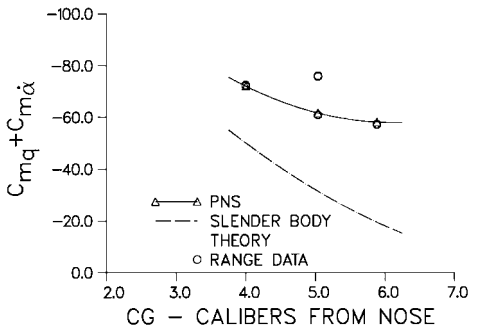

Fig. 17 Variation of pitch-damping moment coefficient sum with c.g. location, M = 2.5, ANSR, L/D = 9.

$\Omega D/V = 0.010$ and a rotational velocity ratio $\Omega R_0/V = 0.0349$, where the linear aerodynamic theory has been shown to be valid.

Figures 12 and 13 show predictions of the pitch-damping moment coefficients C_{m_q} and $C_{m_{\dot{\alpha}}}$, as a function of c.g. position for the $L/D = 5$ and $L/D = 9$ bodies at Mach 2.5. Predictions obtained using the PNS computational approach are shown, along with results obtained with engineering design predictions made with slender-body theory. The results show that the pitch-damping coefficient C_{m_q} is larger than $C_{m_{\dot{\alpha}}}$ for all of the c.g. positions examined. The damping coefficient $C_{m_{\dot{\alpha}}}$ is nearly zero at the rearward c.g. for each of the body lengths. The trends shown by the slender-body results are similar to the PNS results, although the slender-body results are generally lower in magnitude. The predicted variation of C_{m_q} with c.g. position shown in Figs. 12 and 13 agree with the theoretical variation [Eq. (24)] to within 0.25% across the range of c.g. positions examined. The predicted variation of $C_{m_{\dot{\alpha}}}$ is essentially identical to the theoretical variation [Eq. (23)] because the governing equations boundary conditions, and flowfield are independent of the axial c.g. location.

Figures 14 and 15 show similar predictions of the pitch-damping force coefficients C_{N_q} and $C_{N_{\dot{\alpha}}}$, as a function of c.g. position for the $L/D = 5$ and $L/D = 9$ bodies at Mach 2.5. The PNS predictions of the pitch-damping force coefficients show a similar trend to the predictions made with slender-body theory, though the slender-body theory results are larger in magnitude. The agreement does seem to improve slightly as the body length increases.

Because ballistic bodies traverse a nearly rectilinear path, it is impossible to extract the individual components of the damping coefficients from the experimental data. Thus, no comparison of the predicted individual coefficients could be made with experimental data. However, the individual coefficients can be summed to produce the pitch-damping coefficient sum and the results compared with the coning motion results and with experiment. Figures 16 and 17 show comparisons of the pitch-damping coefficient sum (obtained by summing the individual coefficients) with experimental data and with slender-body theory results. The results obtained by summing the predicted coefficients C_{m_q} and $C_{m_{\dot{\alpha}}}$ are within 1.0% or less of the pitch-damping moment coefficient sum predicted using coning motion.

The distribution of the pitch-damping force and moment coefficients over the ANSR $L/D = 5$ body is shown in Figs. 18 and 19. The force coefficient $C_{N_{\dot{\alpha}}}$ is positive along the body length with most of the force being generated at the aft end of the body. As a result, the moment coefficient $C_{m_{\dot{\alpha}}}$ also shows its largest contributions from the aft portion of the body. On the other hand, for the force coefficient C_{N_q}, both the nose and cylindrical afterbody produce contributions to the force coefficient, which are similar in magnitude but opposite in sign. This essentially imposes a couple

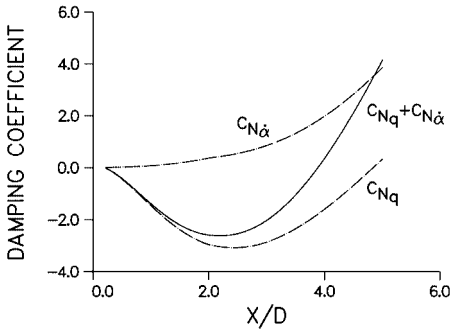

Fig. 18 Development of pitch-damping force coefficients over ANSR body, $M = 2.5$, $L/D = 5$, middle c.g. position.

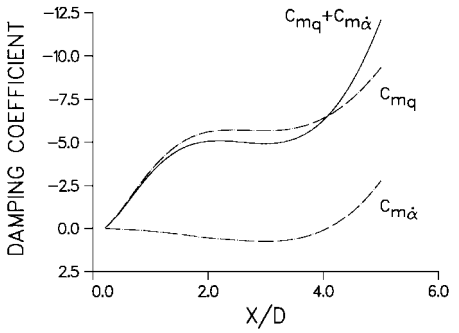

Fig. 19 Development of pitch-damping moment coefficients over ANSR body, $M = 2.5$, $L/D = 5$, middle c.g. position.

on the body whose magnitude is reflected in the moment coefficient C_{mq}.

Conclusion

A method for determining the individual force and moment coefficients that comprise the pitch-damping force and moment coefficient sum has been presented, along with sample results for a family of axisymmetric projectile geometries. The sum of the two individual coefficients is identical to previous predictions of the pitch-damping coefficient sums obtained using coning motion and is in excellent agreement with experimental data. The individual coefficients show qualitative agreement with results obtained using the more approximate slender-body theory. The method provides an efficient means of determining the individual coefficients that may be quite difficult to obtain using experimental means.

References

[1] Schiff, L. B., "Nonlinear Aerodynamics of Bodies in Coning Motion," *AIAA Journal*, Vol. 10, No. 11, 1972, pp. 1517–1522.

[2] Agarwal, R., and Rakich, J. V., "Computation of Supersonic Laminar Viscous Flow Past a Pointed Cone at Angle of Attack in Spinning and Coning Motion," AIAA Paper 78-1211, July 1978.

[3] Lin, T. C., "A Numerical Study of the Aerodynamics of a Reentry Vehicle in Steady Coning Motion," AIAA Paper 78-1358, Aug. 1978.

[4] Weinacht, P., and Sturek, W. B., "Navier–Stokes Predictions of Pitch Damping for Finned Projectiles Using Steady Coning Motion," *Proceedings of the AIAA 8th Applied Aerodynamics Conference*, AIAA, Washington, DC, 1990, pp. 632–642 (AIAA Paper 90-3088, Aug. 1990).

[5] Weinacht, P., Sturek, W. B., and Schiff, L. B., "Navier–Stokes Predictions of Pitch-Damping for Axisymmetric Shell Using Steady Coning Motion," *Proceedings of the 1991 Atmospheric Flight Mechanics Conference*, AIAA, Washington, DC, 1991, pp. 89–100 (AIAA Paper 91-2855, Aug. 1991).

[6] Weinacht, P., "Navier–Stokes Predictions of Pitch-Damping for a Family of Flared Projectiles," *Proceedings of the 9th Applied Aerodynamics Conference*, Vol. 2, AIAA, Washington, DC, 1991, pp. 1025–1034 (AIAA Paper 91-3339, Sept. 1991).

[7] Weinacht, P., "Navier–Stokes Predictions of the Individual Components of the Pitch-Damping Coefficient Sum," *Proceedings of the 1995 Atmospheric Flight Mechanics Conference*, AIAA, Washington, DC, 1995, pp. 291–301 (AIAA Paper 95-3458, Aug. 1995).

[8] Weinacht, P., "Prediction of Pitch-Damping Aerodynamic Derivatives Using Navier–Stokes Computational Techniques," Ph.D. Dissertation, Dept. of Mechanical Engineering, Univ. of Delaware, Newark, DE, Spring 1996.

[9] Qin, N., Ludlow, D. K., Shaw, S. T., Edwards, J. A., and Dupuis, A., "Calculation of Pitch Damping Coefficients for Projectiles," AIAA Paper 97-0405, Jan. 1997.

[10] Murphy, C. H., "Free Flight Motion of Symmetric Missiles," U.S. Army Ballistic Research Lab., Rept. 1216, Aberdeen Proving Ground, MD, July 1963.

[11] Baldwin, B. S., and Lomax, H., "Thin Layer Approximation and Algebraic Model for Separated Turbulent Flows," AIAA Paper 78-257, Jan. 1978.

[12] Schiff, L. B., and Steger, J. L., "Numerical Simulation of Steady Supersonic Viscous Flow," *AIAA Journal*, Vol. 18, No. 12, 1980, pp. 1421–1430.

[13] Beam, R., and Warming, R. F., "An Implicit Factored Scheme for the Compressible Navier–Stokes Equations," *AIAA Journal*, Vol. 16, No. 4, 1978, pp. 393–402.

[14] Rai, M. M., and Chaussee, D. S., "New Implicit Boundary Procedure: Theory and Applications," AIAA Paper 83-0123, Jan. 1983.

[15] Sturek, W. B., and Schiff, L. B., "Computations of the Magnus Effect for Slender Bodies in Supersonic Flight," *Proceedings of the AIAA Atmospheric Flight Mechanics Conference*, AIAA, New York, 1980, pp. 260–280 (AIAA Paper 80-1586, Aug. 1980).

[16] Murphy, C. H., and Schmidt, L. E., "The Effect of Length on the Aerodynamics Characteristics of Bodies of Revolution in Supersonic Flight," U.S. Army Ballistic Research Lab., Rept. 876, Aberdeen Proving Ground, MD, Aug. 1953.

T. C. Lin
Associate Editor